CHEMISTRY OF MATERIALS

ARTICLE

pubs.acs.org/cm

Confirmation of the Domino-Cascade Model by $LiFePO_4/FePO_4$ Precession Electron Diffraction

G. Brunetti,[†] D. Robert,[‡] P. Bayle-Guillemaud,[§] J. L. Rouvière,[§] E. F. Rauch,[▽] J. F. Martin,[‡] J. F. Colin,[‡] F. Bertin,[†] and C. Cayron*[,‡]

[†]CEA, LETI, and [‡]CEA, LITEN, MINATEC Campus, 17 rue des Martyrs, F-38054 Grenoble, France

[§]CEA, INAC, MINATEC Campus, INAC/UJF−Grenoble 1, 17 rue des Martyrs, F-38054 Grenoble, France

[▽]Science et Ingénierie des Matériaux et des Procédés, Université de Grenoble/CNRS, Grenoble INP−UJF, 38402 Saint-Martin d'Hères, France

ABSTRACT: A recent transmission electron microscopy (TEM) method using precession electron diffraction (PED) was used to obtain $LiFePO_4$ and $FePO_4$ phase mapping at the nanometer-scale level on a large number of particles of sizes between 50 and 300 nm in a partially charged cathode. Despite the similarity of the two phases (the difference of lattice parameters is <5%), the method gives clear results that have been confirmed using high-resolution transmission electron microscopy (HRTEM) and energy-filtered transmission electron microscopy/electron energy loss spectroscopy (EFTEM/EELS) experiments. The PED maps show that the particles are either fully lithiated or fully delithiated and, therefore, bring a strong support to the domino-cascade model at the nanoscale level (scale of a particle). A core−shell model or spinodal decomposition at mesoscale (scale of agglomerates of particles) is possible. Size effects on the transformation are also discussed.

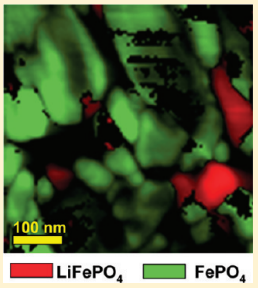

KEYWORDS: lithium batteries, $LiFePO_4$, TEM, phase mapping, precession electron diffraction

1. INTRODUCTION

Lithium iron phosphate ($LiFePO_4$) is a promising material for positive electrodes of lithium-ion batteries of the new generation of electric vehicles. It combines low cost, excellent cycle life, and safety. The number of scientific papers about $LiFePO_4$ has followed an exponential increase since the pioneering work of Padhi et al.,[1] and, as of the beginning of the year 2011, more than 1600 papers on the subject have been published. $LiFePO_4$ material has a theoretical capacity of 170 mAh/g and a reasonably high potential of ∼3.4 V versus Li^+/Li. The main drawback of this material is its low intrinsic electrical conductivity; however, this problem was solved during the past decade using nanoparticles,[2,3] carbon coating,[4,5] doping,[6,7] and/or by controlling off-stoichiometric Li/Fe compositions[8] or Fe/P/O compositions.[9,10] Some of these technical solutions are generally combined to prepare $LiFePO_4/C$ nanocomposite with reversible capacity very close to the theoretical one with cyclability on more than 20 000 cycles,[11] and/or also with very high charging and discharging rate.[9−11] $LiFePO_4$ and $FePO_4$ crystals have an olivine structure (*Pnma*) with lattice parameters $a = 10.33$ Å, $b = 6.01$ Å, and $c = 4.69$ Å for $LiFePO_4$ and $a = 9.81$ Å, $b = 5.79$ Å, and $c = 4.78$ Å for $FePO_4$.[1,12] The projections of these structures along different axes have been reported in many papers (see refs 1 and 6−8 for examples). The $FePO_4$ lattice is an assembly of FeO_6 octahedra sharing corners and forming Fe−O atomic ac planes. The tetrahedral PO_4 units link these planes together, which forms the skeleton of the lattice. Lithium is bounded to the oxygen atoms and diffuses along the *b*-oriented channels between the FeO_6 and PO_4 blocks, as predicted by atomistic calculations,[7,13] and observed by transmission electron microscopy (TEM) by Chen et al.[14] It is possible to elaborate platelet-like shape particles with large *ac* facet and thin part along the *b*-axis.[14,15] Such morphologies are favorable for Li diffusion at high current rates.[15]

Despite its scientific importance, the mechanism of Li insertion in $FePO_4$ or extraction of $LiFePO_4$ is not yet fully understood. It was proven since the work of Padhi et al.[1] that the insertion/extraction of lithium does not proceed via the formation of a continuous solid solution $Li_{1-x}FePO_4$ with $x \in [0,1]$ during the insertion, but actually proceeds via a discontinuous two-phase mechanism:

$$FePO_4 + xLi^+ + xe^- \rightarrow xLiFePO_4 + (1-x)FePO_4$$

The two-phase mechanism was confirmed later in many works (see ref 16, for example). Yamada and co-workers then discovered, by refinement of X-ray diffraction (XRD) data, that the two end-members of the reaction are not the pure compounds $LiFePO_4$ and $FePO_4$ but actually $Li_\alpha FePO_4$ and $Li_{1-\beta}FePO_4$ with $\alpha = 0.032$ and $\beta = 0.038$.[17] Larger values ($\alpha = 0.05$ and $\beta = 0.11$) were deduced by neutron diffraction.[18] It was shown that the domain of solid solution of the two end-members actually depends on the size of the nanoparticles.[19−21] In parallel, using XRD, Delacourt and co-workers could establish the complete phase diagram of Li_xFePO_4, as a function of the lithium content (x) and the temperature (T), and they have shown that Li_xFePO_4 is a solid solution for any $x \in [0,1]$ for $T > 450$ °C.[22] Some metastable phases—$Li_{0.5}FePO_4$, $Li_{0.6}FePO_4$, and $Li_{0.75}FePO_4$—are also reported by cooling the solid solution Li_xFePO_4.[14,22,23]

Received: June 22, 2011
Revised: August 25, 2011
Published: September 21, 2011

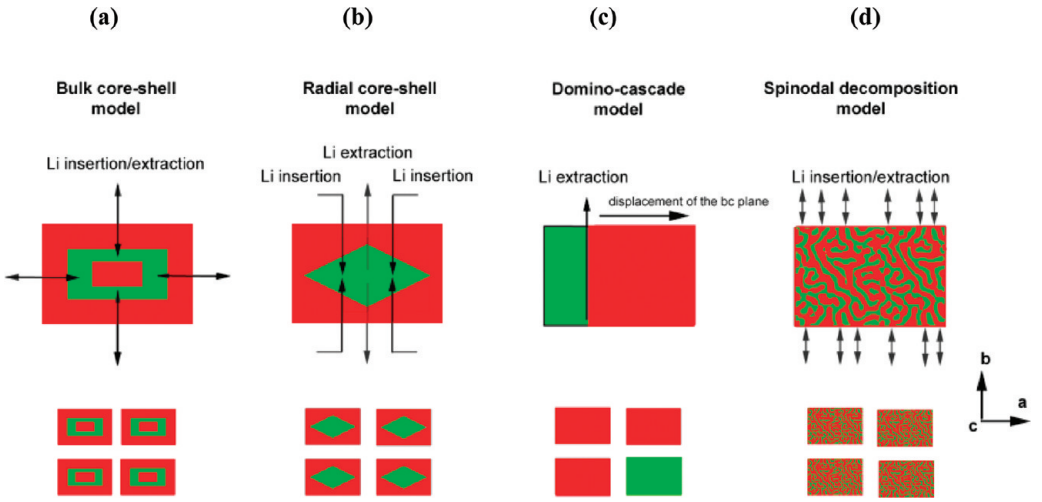

Figure 1. Schematic representations of the $LiFePO_4$ (in red) and $FePO_4$ (in green) phases in the four models proposed in the literature for the Li insertion/extraction mechanisms in $FePO_4/LiFePO_4$ materials: (a) bulk core−shell model,[1,24] (b) radial core−shell model,[26] (c) domino-cascade model,[27] and (d) a fourth model that we have called the spinodal decomposition model freely schematized from ref 29. In all of the models, except the domino-cascade model, the particles are mixed and composed of the two phases.

The controversy among scientists concerns the exact insertion/extraction mechanisms at the microscopic/nanoscopic scale. At least four models (co)exist. The first one, the core−shell model (also called shrinking core model), was deduced by Padhi et al.[1] from their discovery of the two-phase and diffusion-limited character of the Li insertion/extraction process (see Figure 1a). This model was reinforced by Srinivasan and Newman.[24] By electrochemical experiments, they demonstrated an asymmetric behavior between charge and discharge, which was later supported by in situ XRD.[25] They qualitatively explained all of their electrochemical results using the core−shell model, although they already noticed that these are "significantly smaller than those predicted from the model" and that the "shrinking-core model may not be a complete picture of the behavior of the $LiFePO_4$ electrode and some additional features would also need to be considered".[24] Less than one year later, Laffont and co-workers, using electron energy loss spectroscopy (EELS) in TEM show that the Li_xFePO_4 nanoparticles always consist of a $FePO_4$ core and a $LiFePO_4$ shell, regardless of the cycling history of the material,[26] which was in contradiction with the classical core−shell model. They proposed a variant model that we will call the "*radial core-shell model*". It is an anisotropic version of the core−shell model that takes into account the fact that Li diffuses along the *b*-direction, which is normal to the platelet shape of the particle. In that model, during lithiation, the Li ions start to insert in the $FePO_4$ structure by the edges of the particles, and during delithiation, they start to extract from the middle (see Figure 1b). In 2008, Delmas and co-workers created a surprise by proposing a completely different model for Li extraction that they called the *domino-cascade model*.[27] This one results from X-ray diffractions confirming the two-phase transformation, and more interestingly from high-resolution transmission electron microscopy (HRTEM) images, showing that the nanoparticles are either fully lithiated or fully delithiated. In their model, the deintercalation process proceeds via a transversal elastic wave moving through the entire crystal in the *a*-direction while Li ions migrate along the *b*-direction (see Figure 1c). The importance of the elastic deformation during the transformation was already noticed by Padhi et al.[1] and is considered as a primary factor by Meethong et al.[28] The domino-cascade model is a nanoscale model (i.e., at the scale of nanoparticles) and very interestingly, Delmas et al. remarked that "at the agglomerate scale, a core−shell scheme is likely to occur".[27] The relaxation elastic wave associated to delithiation (charge) accelerates the displacement of the $LiFePO_4/FePO_4$ boundaries and by consequence the phase transformation. Therefore, as the two previous models, the domino-cascade model qualitatively explains the asymmetric behavior of the electrode and the fact that charging (delithiation) is easier than discharging (lithiation).[24,25] Another model, which we will call the *spinodal model* (see Figure 1d), was recently proposed by Ramana et al.[29] This model seems to be based on the analogy made by Yamada et al. between the existence of the $Li_\alpha FePO_4$ and $Li_{1-\beta}FePO_4$ solid-solution end-members and a spinodal decomposition.[17] The spinodal model results from experimental HRTEM images, Raman spectroscopy and thermodynamic calculations.

All four models were developed to propose mechanisms at the microscopic/nanoscopic scale. All agree on the two-phase transformation and, therefore, cannot be distinguished by conventional XRD, because of the lack of spatial resolution. In his excellent recent review paper, Zhang stressed that "it is of scientific and engineering importance to understand the Li insertion/extraction mechanisms", and for future research, he proposed the use of "advanced in situ characterization tools".[30] However, in situ experiments used to follow the behavior of a particle seem very tricky. Another way would be to study ex situ, at the nanometer scale, a large number of particles in a partially charged cell in order to obtain statistical information. Conventional electron diffraction or HRTEM techniques are not perfectly appropriate for that purpose, because they require a time-consuming manual tilting of the particles in order to orientate them correctly along a low-index zone axis, and laborious indexation work of the diffraction patterns or power spectra of the HRTEM images. Local differentiation of the phase can be obtained by EELS by considering either the exact position of the Fe $L_{2,3}$ peaks or the existence or absence of a prepeak located few eV before the O−K peak,[26] or the existence/absence of a peak in the 4−7 eV range of the valence spectrum characteristic of $FePO_4$.[31] However, EELS experiments for mapping are time-consuming and are often restricted to small particles to avoid

dx.doi.org/10.1021/cm201783z |*Chem. Mater.* 2011, 23, 4515–4524

Table 1. Lattice Parameters of the $LiFePO_4$ and $FePO_4$ Phases, and Position of Unique Atoms Given in Terms of Fractional Coordinates (x, y, z), Corresponding to $xa + yb + zc$

	a [nm]	b [nm]	c [nm]	α, β, γ [deg]	element	position	ref
$LiFePO_4$	1.033	0.601	0.469	90	Li	(0.00, 0.00, 0.00)	1
					Fe	(0.28, 0.25, 0.97)	
					P	(0.09, 0.25, 0.42)	
					O_1	(0.16, 0.05, 0.28)	
					O_2	(0.45, 0.25, 0.21)	
					O_3	(0.09, 0.25, 0.74)	
$FePO_4$	0.981	0.579	0.478	90	Fe	(0.27, 0.25, 0.95)	12
					P	(0.09, 0.25, 0.40)	
					O_1	(0.17, 0.04, 0.25)	
					O_2	(0.44, 0.25, 0.15)	
					O_3	(0.12, 0.25, 0.71)	

thickness effects. This paper introduces a recent TEM technique based on precession electron diffraction (PED) and clearly shows that this one allows distinguishing the $LiFePO_4$ and $FePO_4$ phases, despite their very close lattice parameters. Phase maps of $LiFePO_4$ and $FePO_4$ at the nanometer scale on a large number of particles are automatically produced. The results are supported by HRTEM and EELS experiments. Statistical information extracted from the PED automatic phase mapping will allow us to discriminate the four models that have been proposed in the literature.

EXPERIMENTAL SECTION

Materials. This study was carried out on three samples: two single-phase samples and a partially electrochemically delithiated $LiFePO_4$ sample. The structure of the $LiFePO_4$ and $FePO_4$ phases is described in the *Pnma* space group with crystallographic data summarized in Table 1. The difference between the lattice parameters of both phases is 5.0% for lattice parameter *a*, 3.7% for lattice parameter *b*, and −1.9% for lattice parameter *c*. Because of this weak difference, the interplanar distances are very close (see Table 2) and the diffraction patterns look quite similar. However, as it will be shown, the differentiation between the phases can be done through the positions and intensities of the diffraction, using the precession technique.

The single-phase samples have been prepared according to the following process. A $LiFePO_4$−C composite was synthesized via a preliminary mechano-chemical activation of the precursors and then via a thermal treatment of this mixture. The reactants—iron phosphate $(Fe_3(PO_4)_2 \cdot 6.5H_2O)$ and lithium phosphate (Li_3PO_4)—were mixed with 10 wt % cellulose in order to create a carbon coating. This precursor mixture was ball-milled four times for 1 h each time in a planetary mill, using tungsten carbide vessels and 10-mm-diameter agate balls. The resulting mixture was thermally treated in a tube under an argon flow, which was introduced in a tubular furnace already at 600 °C for 15 min. $LiFePO_4$ was used as a raw material for the preparation of $FePO_4$ via chemical oxidation. $LiFePO_4$ (520 mg) was reacted with an excess of nitronium tetrafluoroborate (NO_2BF_4) in acetonitrile to form 500 mg of $FePO_4$. The reaction was realized under an argon gas flow for 60 h, and then this mixture was filtering and dried under vacuum at 60 °C. This product was controlled using XRD (not shown here), and no impurity could be detected.

The partially charged samples were prepared by electrochemical oxidation of $LiFePO_4$, yielding Li_xFePO_4 ($x = 0.5$ theoretically). Electrodes were prepared from a 500-mg mixture of 80 wt % of C−$LiFePO_4$ active material with 10 wt % Super P carbon black (Timcal) and 10 wt % polyvinylidene difluoride (PVdF) binder (Solef 1015, Solvay) in *N*-methylpyrrolidone (NMP). This mixture was then cast onto an aluminum foil and dried overnight at 55 °C. Discs 14 mm in diameter were finally punched, pressed at 6.5 T cm^{-2}, and dried for 48 h at 80 °C under vacuum. These electrodes were weighed with 5 mg of active material. The negative electrode is a disk of lithium metal foil. Two separators in polypropylene wetted by the liquid electrolyte in a mixture of propylene carbonate/ethylene carbonate/dimethyl carbonate (1:1:3) containing $LiPF_6$ as salt (1 mol L^{-1}) were placed between the two electrodes.

Table 2. List of the Interplanar Distances (d_{hkl}) in $LiFePO_4$ and $FePO_4$

	Interplanar Distance, d_{hkl} (Å)	
hkl[a]	$LiFePO_4$	$FePO_4$
100*	10.33	9.81
010*	6.01	5.79
110*	5.19	4.98
200	5.16	4.90
001*	4.69	4.78
101	4.27	4.30
210	3.92	3.74
011	3.70	3.68
111	3.48	3.45
201	3.47	3.42
300*	3.44	3.27
211	3.00	2.94
020	3.00	2.89
310*	2.99	2.85
120*	2.88	2.77

[a] The asterisk symbol (*) means that the diffraction spots should be extinguished by the structure factor but can be visible in the diffraction patterns or power spectra due to dynamical effects (double diffraction).

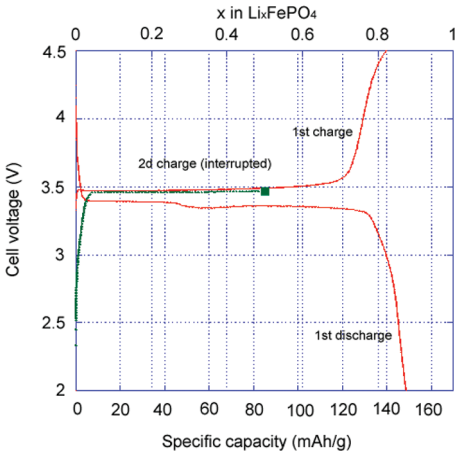

Figure 2. Charge/discharge galvanostatic profile of composite Li_xFePO_4−C obtained under normal cycling conditions (20 °C, C/20 rate). $x = 0.5$ for theoretical lithiation. The first charge and discharge are shown in red, and the second charge (interrupted) is shown in green. One may notice a slight difference of capacity between the charge and discharge, which comes from a slight oxidation of the $LiFePO_4$ powders (thus partially transformed into $FePO_4$) during their elaboration (drying in bad vacuum). The capacity completely recovered at the end of the first discharge.

dx.doi.org/10.1021/cm201783z |*Chem. Mater.* 2011, 23, 4515–4524

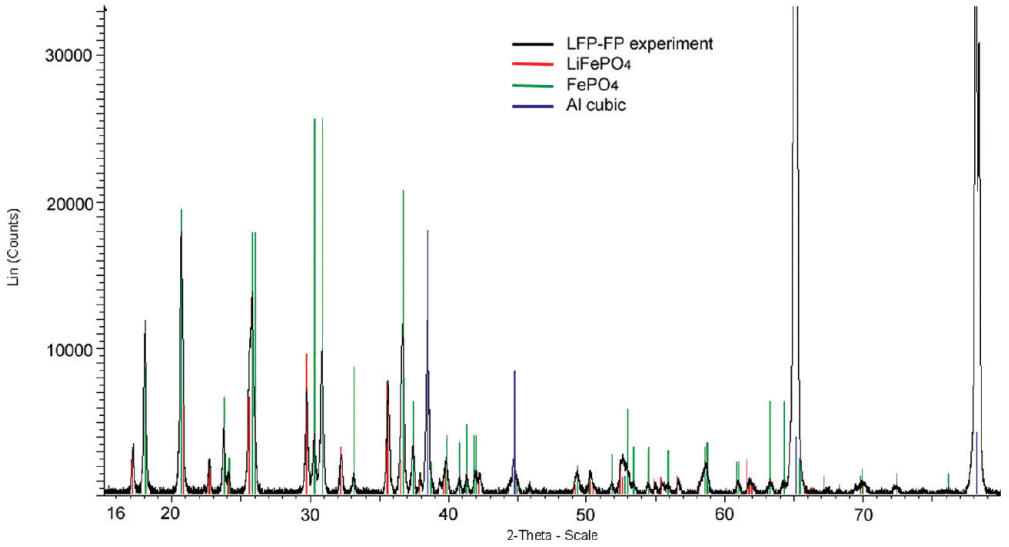

Figure 3. X-ray diffraction (XRD) diagram of the powder in the partially charged cell. The theoretical lines of $LiFePO_4$ are shown in red, and the theoretical lines of $FePO_4$ are shown in green. The Al lines are shown in blue.

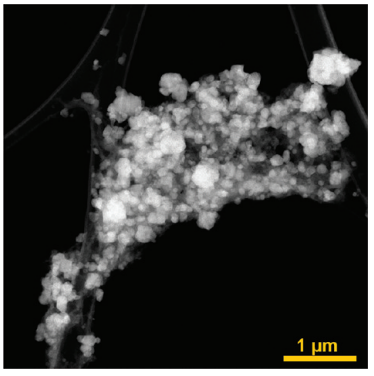

Figure 4. Scanning transmission electron microscopy (STEM) image in dark-field mode of the particles repartition in the mixed sample.

These lithium cells were assembled in a drybox under argon. Lithium extraction/insertion was monitored with Arbin Model BT/HSP-2043 automatic cycling data recording system (Arbin, College Station, TX, USA), operating in galvanostatic mode, at C/20 rate. Results at the first discharge are in agreement with the literature (150 mAh g^{-1} at C/20), showing that all particles were involved in the electrochemical process (only a slight oxidation of the initial powders has been impeded to reach this capacity at the first charge). The second charge stopped to 84.9 mAh g^{-1}, corresponding to an expected $FePO_4/LiFePO_4$ ratio of 50%. The charge/discharge galvanostatic profile of composite Li_xFePO_4−C is given in Figure 2. After cycling, the cell was relaxed for 24 h at open circuit voltage. The lithium cells were disassembled in a drybox under argon. Positive electrodes were washed with dimethyl carbonate and dried under argon gas. The XRD diagram of the powder in the partially charged cell is reported in Figure 3. The actual $FePO_4/LiFePO_4$ ratio calculated by Rietveld refinements of the X-ray diagram with Fullprof software is 61% $FePO_4$ and 39% $LiFePO_4$. The powders were also dispersed on copper grid with carbon membrane for their analysis via TEM. The repartition of the particles is represented in Figure 4. The size of the particles comprising the powder is 50−300 nm. Since Li_xFePO_4 are sensitive to air moisture,[32] the powders were stored in a box connected to a primary vacuum pump to avoid as much contact with air as possible.

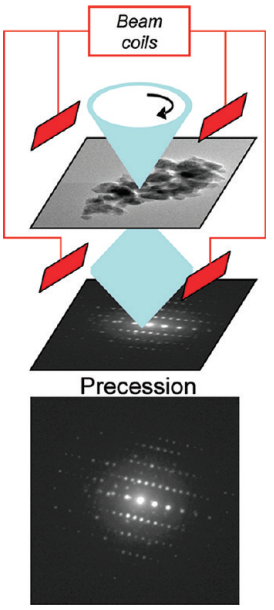

Figure 5. Schematic representation of the precession electron diffraction (PED) technique.

Techniques. An automated phase mapping tool for TEM is used in the present study. The technique was initially developed for orientation mapping[33−35] and recently extended to promote automatic phase mapping with a TEM system.[36] The full hardware and software attachment is currently commercialized under the name ASTAR by the NanoMEGAS company.[37] This tool makes use of two complementary techniques: (i) precession electron diffraction (PED)[38] and (ii) template matching.[33]

For PED, the incident electron beam is focused, tilted, and rotated in a conical fashion at the sample surface. The diffraction pattern is averaged as the beam rocks about the optic axis. To compensate for the movement of the diffraction pattern, the diffracted beams are tilted in a complementary way, so that the diffraction pattern appears as a stationary spot pattern, as shown in Figure 5. The rotation angle is called the precession angle. The intensity within diffraction discs are integrated over a range of angles that includes the Bragg angle, and thus are very close to kinematical

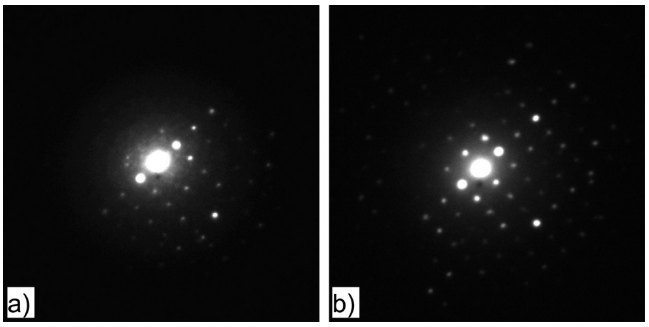

Figure 6. Diffraction patterns of the same $FePO_4$ particle acquire (a) without precession and (b) with a precession angle of 0.96°.

intensities,[38] even if double diffraction and "forbidden" spots can appear for thick TEM foil and/or heavy material. The PED patterns are collected with a charge-coupled device (CCD) camera while the area of interest is scanned by the electron beam. The precession unit is operated at 100 Hz, so that up to 100 PED patterns may be acquired per second and stored in the computer memory.

The template matching process is essentially an image correlation technique: local crystallographic orientation and/or phase are identified through an algorithm that compares the recorded PED patterns with precalculated (simulated) templates for all possible orientations and phases. The orientation and phase identification is currently performed off-line with a limited number of templates: exploring the orientation space of one phase with an angular resolution of 1° generates <2000 simulated templates (for cubic crystals), which is generally sufficient to identify an orientation. The degree of matching between experimental patterns and simulated templates is given by a correlation index. The highest value corresponds to the adequate orientation/phase. More details are given in ref 36.

For this study, we have used an ASTAR system installed on JEOL Model 2010-FEF TEM system operating at 200 kV. The precession module is a recent version called DigiSTAR.[37] An external "fast optical" CCD camera AVT Stingray was used for the acquisition of the PED patterns. They were recorded as 144 × 144 pixel images with 8-bit dynamical range. The external position of the camera introduces some distortions in the diffraction patterns that are corrected during the data treatment. The camera length and the distortions are calculated using a silicon sample oriented along the [110] direction as the reference sample. These parameters are kept constant for the treatment of maps acquired during the same session (typically for a day). The noise in the PED patterns is reduced by the application of different filters. In our study, the PED patterns have been obtained with a 10-μm condenser aperture, a convergence angle of 0.6 mrad, a camera length of 60 cm, and a spot size (diameter) of 2.6 nm (full width at half-maximum) without precession and 2.7 nm with a precession angle of 0.96°. This angle was chosen because it offers enough intensity for the diffraction spot and also enough information in the reciprocal space. An example of the diffraction pattern with and without precession is shown in Figure 6. Several maps of PED patterns have been acquired using a step size of 5 nm for a region of interest of 500 nm × 500 nm, which allows the study of a large number of particles. Each PED pattern is acquired within <0.2 s, and the acquisition of a map lasts ~33 min. The maps presented in this study have been recorded during different working sessions but with the same experimental conditions.

For each map, the experimental PED patterns are compared to the theoretical templates and indexed with a submodule of ASTAR called Index. In order to distinguish the $LiFePO_4$ and $FePO_4$ phases, the databank should contain as much simulated PED templates as possible. However, a very high number drastically increases the calculation time. Different tests have been performed, and a good compromise was obtained for template banks containing 5151 patterns, which corresponds to an angular step of ~0.3° between each simulated pattern. For each experimental pattern, the correlation index (Q) is calculated as follows:

$$Q_i = \frac{\sum_{j-1}^{m} P(x_j, y_j) T_i(x_j, y_j)}{\sqrt{\sum_{j-1}^{m} P^2(x_j, y_j)} \sqrt{\sum_{j-1}^{m} T_i^2(x_j, y_j)}}$$

where $P(x,y)$ and $T_i(x,y)$ are the intensity functions of the experimental and simulated patterns, respectively. The highest Q value corresponds to the most probable solution to index the experimental pattern. After comparing the experimental pattern with all the simulated ones, a phase reliability index (R) is determined between the two highest optimum solutions (one per phase, $Q_1 = Q$ and Q_2) using the formula

$$R = 100\left(1 - \frac{Q_2}{Q_1}\right)$$

The parameters Q and R are important for estimating the confidence of the phase identification. The parameter Q is used as a threshold to remove pixels in the phase map coming from poor-quality diffraction patterns due to overlapping of several diffraction patterns when particles overlap. The reliability index (R) is used to remove the patterns where the indexation between both phases is too close. The phase maps presented in this work were all filtered with the same parameters Q and R: only pixels in the maps with a correlation index of $Q > 200$ and a reliability index of $R > 5$ are considered, and the other pixels are assumed to contain no information and are not taken into account. The post-treatment of each map lasts 3 h.

This treatment allows us to transform a series of PED patterns into either an orientation map, a phase map, a correlation index map, a reliability index map, or some superimpositions of them.

The PED phase mapping brings a lot of statistical information on a high number of nanoparticles. Since this technique is recent, we have checked its validity by HRTEM and EELS on a more-limited number of nanoparticles observed in the same TEM samples. The HRTEM observations have been performed on a FEI image Cs-corrected Titan Cube TEM system operating at 200 kV. Energy-filtered transmission electron microscopy (EFTEM) has been performed at 200 kV on the same microscope equipped with a Tridiem Gatan Imaging Filter. Series of EFTEM images with an energy selecting slit of 1 eV have been acquired to fill the so-called data cube (x,y,ΔE), ΔE being the electron energy loss and x and y denoting the position in the image. The EELS spectra were reconstructed from these stacks of EFTEM images using Digital Micrograph module "Spectrum Imaging". The XRD diagrams have been obtained with a Bruker D8 diffractometer, $\theta-2\theta$ geometry, back monochromator, using Cu Kα radiation (λ = 1.54056 Å).

RESULTS

Validation of the PED Technique on Pure Powders. The validation of the PED method for phase identification was achieved by the mapping of single-phase $LiFePO_4$ and $FePO_4$ powder samples. Both samples were studied during different working sessions, according to the same experimental conditions defined previously. Four different maps were acquired: two for $LiFePO_4$ and two for $FePO_4$. Each map was indexed by considering the templates of $LiFePO_4$ and of $FePO_4$ phases, without giving any preference to the software. In this way, the method can be checked and an error bar associated to this method can be determined. An example for the phase identification of the single-phase $FePO_4$

dx.doi.org/10.1021/cm201783z |Chem. Mater. 2011, 23, 4515–4524

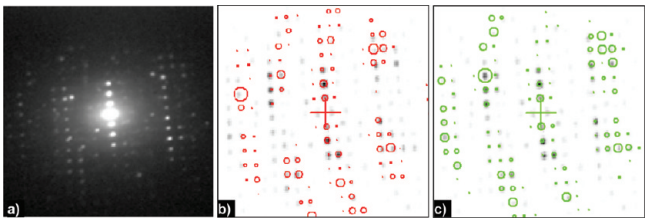

Figure 7. (a) Experimental PED pattern acquired on a single-phase $FePO_4$ sample for a precession angle of 0.96° and its indexation according to (b) the $LiFePO_4$ template (correlation index Q = 554) and (c) $FePO_4$ templates (correlation index Q = 658). The circles in colors correspond to the fitted orientation (red for $LiFePO_4$ and green for $FePO_4$). Clearly more spots are well positioned in panel (c) than in panel (b).

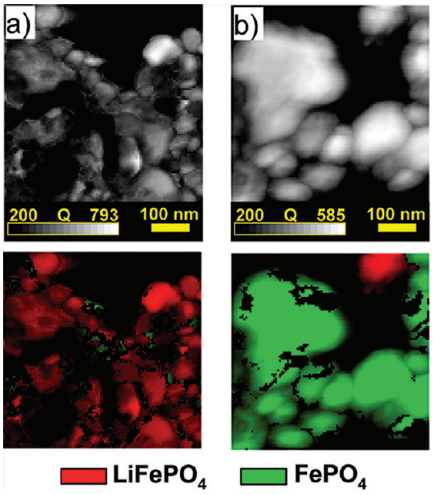

Figure 8. Examples of phase identification for (a) the $LiFePO_4$ sample and (b) the $FePO_4$ sample. Top images show index correlation maps; bottom images show the corresponding phase maps.

sample is given in Figure 7. The PED pattern of one particle is presented in Figure 7a; its best fit with the $FePO_4$ templates gives Q = 658, whereas its best fit with the $LiFePO_4$ templates gives Q = 554, which allows us to conclude that the particle is $FePO_4$, as expected, and, moreover, with a comfortable reliability ($R \approx 15$). Both positions and intensities of the PED spots were taken into account for the fit, which explains the success of the PED phase identification, despite the similarities of the $LiFePO_4$ and $FePO_4$ phases. This analysis is automatically performed by the software for all pixels of the map: the pixels with $Q < 200$ and $R < 5$ are plotted in black (no sufficient information), and for the other ones, the pixels are plotted in red (if $Q(LiFePO_4) > Q(FePO_4)$) or green (if $Q(FePO_4) > Q(LiFePO_4)$). Examples of phase maps obtained for the pure $LiFePO_4$ and for $FePO_4$ powder samples are presented in Figures 8a and 8b, respectively. More than 93% of the pixels above the R and Q thresholds are identified to the expected phase, i.e. $LiFePO_4$ for the $LiFePO_4$ sample and $FePO_4$ for the $FePO_4$ sample. The exact values for four maps are reported in Table 3. This analysis shows that the PED technique allows $FePO_4$ for the $FePO_4$ phase mapping within a mean error bar of ~6%.

PED Phase Identification on a $LiFePO_4$/$FePO_4$ Mixed Sample. The phase identification by PED was applied on a mixed sample coming from the partially charged lithium cell

Table 3. Quantification of the Phase Identification by PED Phase Mapping for Single-Phase Samples

sample		indexation of $LiFePO_4$ [%]	indexation of $FePO_4$ [%]
pure $LiFePO_4$	map 1	94.3	5.6
	map 2	95.6	4.3
pure $FePO_4$	map 3	6.7	93.2
	map 4	5.9	94.0

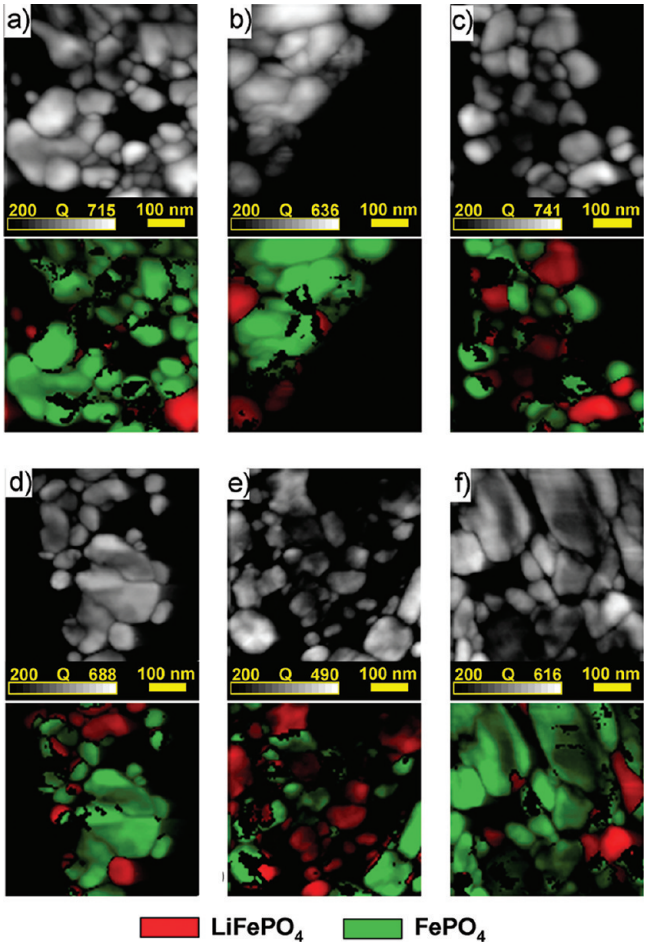

Figure 9. Six PED phase maps acquired within the partially charged lithium cell sample; the proportion of $FePO_4$ is (a) 89%, (b) 80%, (c) 56%, (d) 75%, (e) 44%, and (f) 87%. Top images show correlation maps; bottom images show the corresponding phase maps with the ($Q > 200$, $R > 5$) filter. The particles are fully lithiated or fully delithiated. Only a few particles appear mixed in panel (d).

described in the Experimental Section. The crucial question we want to answer is this: Are the particles composed of a mixture of both phases or are they completely lithiated or delithiated? To carry out the study, six regions of interest were mapped (500 nm × 500 nm, step size = 5 nm) during the same working session and for the same experimental conditions (spot size of 2.7 nm and precession angle of 0.96°). The same camera length, distortions, and image treatment and filter ($Q > 200$, $R > 5$) have been applied to the PED patterns. The six phase maps are reported in Figure 9. Each map contains more than 30 particles. Some maps are mainly composed of $FePO_4$ particles, and others are

dx.doi.org/10.1021/cm201783z |*Chem. Mater.* 2011, 23, 4515–4524

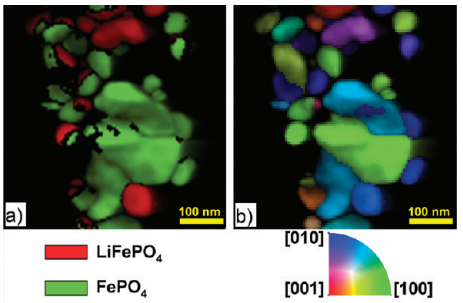

Figure 10. (a) PED phase map (panel d in Figure 9) and (b) the corresponding orientation map. Color coding is given below each image.

more balanced. By averaging the proportions of phases on the six maps, it was found that the powders are composed of 71% $FePO_4$ and 29% $LiFePO_4$. The PED images show that most of the particles are either fully $LiFePO_4$ or fully $FePO_4$ and are not mixed. Also note that most of the big particles are $FePO_4$. The few mixed particles (two in Figure 9d and one in Figure 9e) are among the smallest ones; they are composed of two $LiFePO_4$/$FePO_4$ parts separated by a straight boundary and do not exhibit a core−shell structure. An orientation map corresponding to Figure 9d is also reported in Figure 10b. Careful examination at the mixed particles in this figure show that they are monocrystalline, with a coherent interface boundary between the $LiFePO_4$ and $FePO_4$ parts, which means that these mixed particles were monocrystalline before delithiation.

We have also tested the robustness of the PED method by adding a hypothetical intermediate phase in the treatment of the six phase maps while keeping the same threshold parameters Q and R. A hypothetical $Li_{0.5}FePO_4$ phase was created (solid solution with lattice parameters obtained by averaging those of $LiFePO_4$ and $FePO_4$ phases, and a Li occupancy of 0.5). This phase has been added to the $FePO_4$, $LiFePO_4$ phases in the databank. Here, it is just used for the test and has no real significance, since it was not detected by XRD. The results (not shown here) are very similar to those of Figure 9 with only a larger black area in some particles, due to a lower R value (~20% increase of the black area) and very limited parts of few particles (wrongly) identified as being the artificial $Li_{0.5}FePO_4$ phase (representing <3% of the other phases). This test reinforces the validity of the PED phase mapping method, even for similar phases with a difference in lattice parameters of <5%.

Confirmation by HRTEM. The same sample has been studied by HRTEM. Five particles could be orientated along a low-index zone axis. Only such low-index HRTEM images can be used to discriminate between the $LiFePO_4$ or $FePO_4$ phases. All the images show a homogeneous structure; neither core−shell, nor amorphous interface between two $LiFePO_4$ and $FePO_4$ domains (Figure 4 of ref 14), nor spinodal region (Figure 6 of ref 29) could be observed. Only continuous variations of the contrast appear, because of the thickness gradients of the particles. For each particle, some HRTEM images were acquired at the center and on the edges. All exhibit exactly similar power spectra (i.e., the modulus part of their fast Fourier transform (FFT)), with peaks at exactly the same positions (or a slight rotation without distortion, if a subgrain boundary exists in the particle). Only the HRTEM images acquired on the edge of the particles are reported here in Figure 11. These five HRTEM could be indexed by considering the spots at high frequencies (corresponding to a

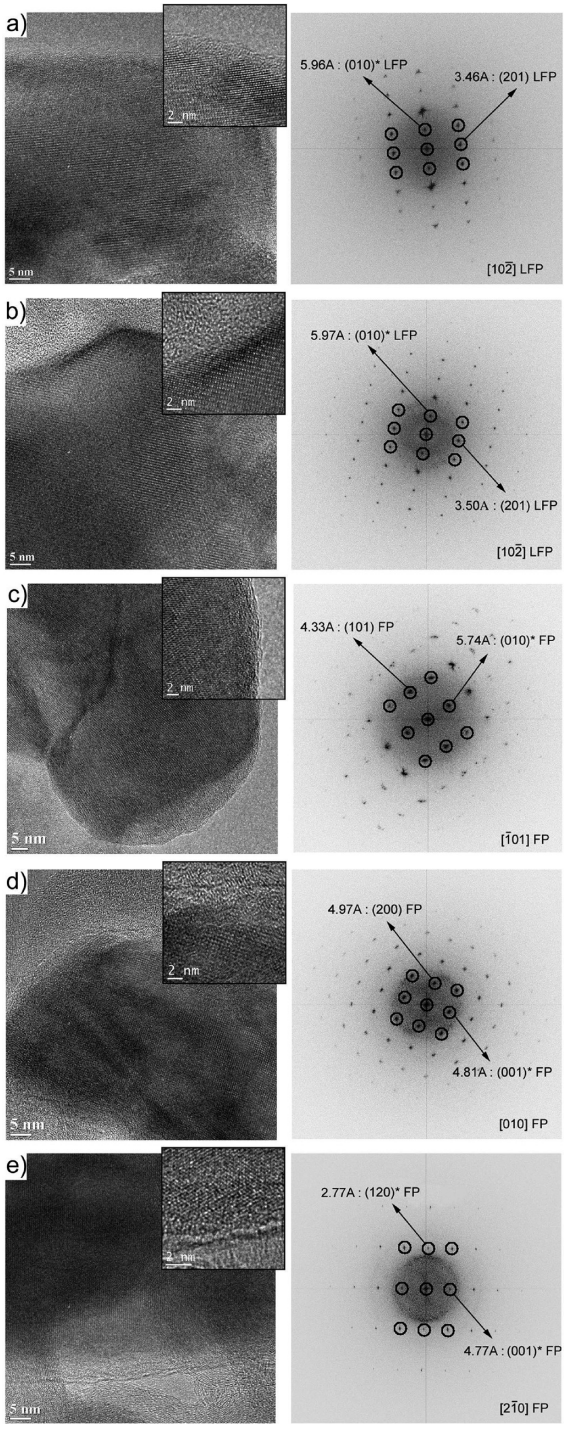

Figure 11. HRTEM images of particles in the partially charged sample acquired on the image Cs-corrected Titan TEM system at 200 kV (with enlargements of a part of the surface in the insets of the top right corners), and the corresponding power spectra. (a,b) Particles identified as pure $LiFePO_4$ and (c−e) particles identified as pure $FePO_4$. The asterisk symbol (*) means that the spot should be extinguished due to the structure factor but is actually visible by dynamical effect. LFP = $LiFePO_4$ and FP = $FePO_4$. The interplanar distances are measured in Angstroms. The discrepancies between the measured and theoretical distances are (a) 0.5% and (b) 0.8% with the LFP phase, and (c) 0.9%, (d) 1.0%, and (e) 0.1% with the FP phase. They would have been far worse with the bad indexation (FP ↔ LFP): (a) 2.2%, (b) 2.7% with the FP phase, and (c) 3.5%, (d) 3.1%, and (e) 2.9% with the LFP phase.

dx.doi.org/10.1021/cm201783z |*Chem. Mater.* 2011, 23, 4515–4524

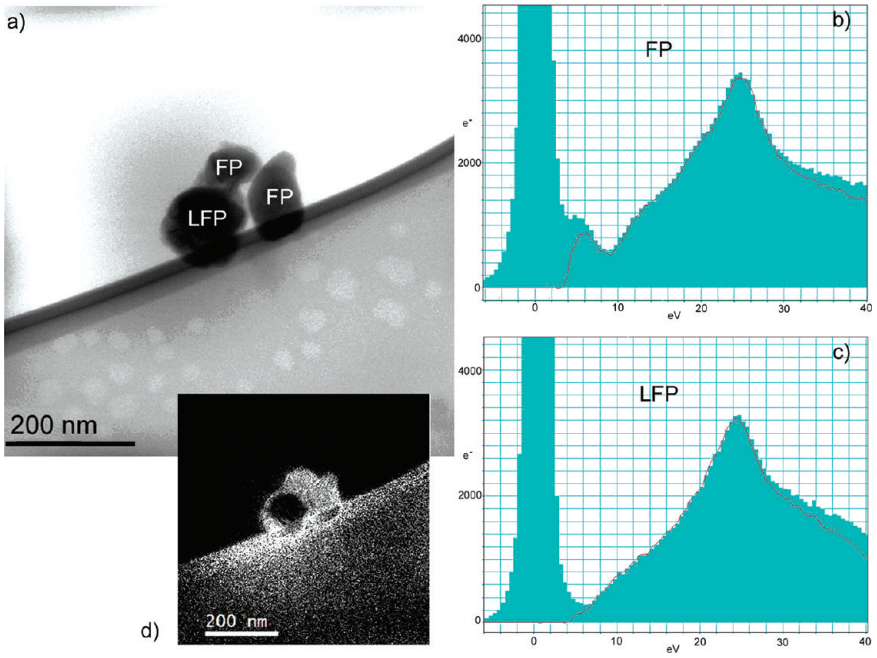

Figure 12. EFTEM and EELS results on three particles in the partially charged sample agglomerated in the vacuum at the edge of the support carbon film of the TEM grid. (a) Elastic image (filtered on the zero-loss peak), (b) reconstructed EELS spectrum of a $FePO_4$ particle, and (c) reconstructed EELS spectrum of a $LiFePO_4$ particles. The continuous red line corresponds to the spectrum obtained after removal of the continuous background of the zero-loss peak. The inset in panel (d) shows the EFTEM image obtained for a slit centered at 5 eV. The white particles correspond to the $FePO_4$ phase, and the black particle correspond to the $LiFePO_4$ phase. The carbon film and the carbon coating around the particles also appear white, because of the higher background in the EELS spectra.

resolution of better than 1 Å). The distinction between pure $LiFePO_4$ and pure $FePO_4$ phases is unambiguous. Manual indexations with an error bar of <1% (on average) are obtained by choosing the good phases and above 3% in average by choosing the wrong phases. The five power spectra have been also indexed automatically with ASTAR, leading to the same phase identification with quality index $Q > 450$ for all the FFT (except the FFT of Figure 11c, for which $Q = 117$) and reliability index $R > 8$. These HRTEM images confirm the PED results: the particles are either fully lithiated or fully delithiated. Moreover, other details can be noticed. As shown in Figures 11a−c, the amorphous layer at the surface of the particles is very thin (<2 nm). Thicker layers (5−10 nm) are visible in some HRTEM images (Figures 11d and 11e), but they are systematically associated to carbon ions, which suggests that theses thick layers are the carbon coating and not amorphous $LiFePO_4$ or $FePO_4$. Very few dislocations or subgrain boundaries could be observed; one is shown in Figure 11c.

Confirmation by EELS. The same samples have also been studied by EFTEM and EELS. Different zones have been chosen where the particles were not overagglomerated. Forty five (45) EFTEM images between −5 and 40 eV with a 1 eV slit have been acquired and stacked. The EELS spectra are reconstructed from these stacks by measuring the mean intensity in an area of interest in the images (typically a square with dimensions of 30 nm × 30 nm). The areas of interest were chosen in different particles, at the center or at the edge, etc. Some images and examples of reconstructed EELS spectra are presented in Figure 12. Clearly, some particles exhibit a peak close to 5 eV and other particles do not exhibit this peak, whatever the location of the area of interest (center or edged). This observation is confirmed by the good homogeneity of the contrast inside the particles in the EFTEM images obtained at 5 eV. Moreau et al.[31] have already noticed that point and they showed by simulations that the presence/absence of that 5 eV peak corresponds to the $FePO_4/LiFePO_4$ phases, respectively. Our observations confirm Moreau et al. results, and again, reinforced the experimental evidence for fully lithiated or fully delithiated states of the particles.

DISCUSSION

This study shows that the PED phase mapping brings reliable and statistical information at the nanometer scale on the spatial distribution of the $LiFePO_4$ and $FePO_4$ phases. PED showed that the powders are composed of 71% $FePO_4$ and 29% $LiFePO_4$, which is in agreement with the macroscopic proportion of 61% $FePO_4$ and 39% $LiFePO_4$ obtained via XRD. However, the proportion of delithiated particles is higher than expected by electrochemistry (50%). It is possible that the diffraction properties (coherence length) of the big $FePO_4$ crystals might favor their proportions in the XRD results over the smaller $FePO_4$. A nonlinear behavior of phase transformation has already been observed by Leriche et al.[39] via XRD in operando studies, but this was observed at high charging rates and their results (a delay in the $FePO_4$ formation) were opposite to ours.

More than 150 particles have been mapped, and it appears that >95% of them are either fully lithiated or either fully delithiated. This statistical result was confirmed by HRTEM and EFTEM/EELS characterizations on a more-limited number of particles. We conclude that the domino-cascade model is confirmed experimentally, or at least its foundation, i.e., the fully lithiated or delithiated state of the particles after partial delithiation. This is an important experimental result, because the domino-cascade model was established by Delmas and co-workers, based on a very limited number of HRTEM images.[27] Now, a new

dx.doi.org/10.1021/cm201783z |*Chem. Mater.* 2011, 23, 4515–4524

question is raised: How does one consider the experimental results of Srinivasan and Newman,[24] which show the importance of the cycling history on the electrochemical behavior of $LiFePO_4$ electrodes, which led them to adopt the core−shell model? Actually, as reported by Delmas et al.[27] and Moreau et al.,[31] we think that the domino-cascade model explains the mechanism at the particle scale, but the bulk core−shell or spinodal decomposition model are likely to occur at an agglomerate scale (mesoscale). The tendency to form agglomerates of fully lithiated particles and agglomerates of fully delithiated particles during charging cycles appears on some images, as observed in Figure 9e, but it is just a statistical tendency, not a strict rule, as shown in the other panels of Figure 9.

The PED phase maps allow us to bring further information. Indeed, it has been noticed in the partially charged cell that the largest particles are almost systematically delithiated. This means that, during charging, the large particles start delithiating before the small ones. This result is consistent with the observation by Lee et al.,[40] that, with a system composed of heterogeneous particle size distribution, at low current density, "larger particles will be delithiated first" (XRD shows that bulk $LiFePO_4$ mixed with nano-$FePO_4$ spontaneously delithiate via ionic transports to transform nano-$FePO_4$ into nano-$LiFePO_4$). The Lee et al.[40] results are consistent with those from previous works by Meethong et al.,[19,28] showing a slight increase of the plateau voltage with decreasing particles size. Lee et al. interpreted their results using a size effect on the electrochemical potential, with reference to a paper by Jamnik and Maier.[41] However, a "simple" size effect would lead to the opposite effect. Indeed, reducing the size of the particle would lead to an increase of the free energy,[41] and, thus, to a *negative* change of the equilibrium potential,[42]

$$\Delta\varepsilon = -\frac{2\gamma v_m}{nF}\left(\frac{1}{r}\right) \quad (1)$$

with $\Delta\varepsilon$ being the difference in electrochemical potential between nano and bulk particles, r is the particle size, γ is the surface energy, v_m is the molar volume of the particle, n is the number of moles of electrons transferred during the reaction, and F is the Faraday constant. Actually, eq 1 can be applied to ion/metal couples and not directly to solid/solid electrochemical couples. The size effect on the chemical potential is more complex and one should take into account the difference in surface energy of the $LiFePO_4$ and $FePO_4$ phases, the size effect on Li solubility,[19−21] the environment (electrolyte and surface coating), and, more importantly, the coherency strain energy. A complete theoretical study including the strain energy on the electrochemical potential (with comparisons with experimental data) does not yet exist, even if interesting works have begun to clarify some points.[28,43] The strain effect can be imagined as follow: the smaller the particle, the easier the strain relaxation of the elastic interface by the surface. Moreover, it has been reported by XRD and by galvanostatic tests that small particles (<100 nm) have a larger miscibility gap than larger ones.[19−21] If one imagines a two-phase mixed particle, the elastic misfit barrier associated to the interface between the two end-member Li_xFePO_4 and $Li_{1-x}FePO_4$ domains inside the particle is smaller for small particles than for large ones, because the difference of lithium content between the two domains $(1 - 2x)$ is smaller. These arguments make us think that small $LiFePO_4/FePO_4$ mixed particles are thermodynamically more stable than large ones if we make the hypothesis that the free energy is dominated by the interfacial strain energy. This point is supported by the PED phase maps showing that the few mixed particles are smaller than the monophase particles. The importance of the strain energy at the $LiFePO_4/PO_4$ interface is at the heart of the domino-cascade, but, contrary to Delmas et al.,[27] we do not think that "the smaller the particle size, the faster the boundary displacement".[27] The strain effect should, in fact, be more pronounced with large particles than small ones.

Regarding the rate capacities of the batteries, the use of small particles seems to lead to two opposite effects. On one hand, according to Meethong et al.,[28] nanoparticles have a positive effect: the expansion of solid solution domains around the end-members Li_xFePO_4 and $Li_{1-x}FePO_4$ increases the coexistence of Fe^{2+} and Fe^{3+} and the changes in lattice parameters should be expected to increase the electronic conductivity and possibly influence the ionic conductivity, and, more importantly, it is possible to retain coherent interface, which provides "facile" (i.e., high rate) transformation. Larger particles should contain incoherent interface with strain accommodating dislocations that limit the rate capacity of the particles. In other words, it is suggested that relief of the misfit strain using nanoparticles facilitates high rate capability.[20] On the other hand, elastic energy between the Li_xFePO_4 and $Li_{1-x}FePO_4$ domains inside a particle is the driving force of the fast transformation in the domino-cascade model. Actually, one of the two opposite effects probably dominates the other one, depending on the cathode material. From our observations and the literature, it seems that the domino-cascade mechanism is the predominant effect in $LiFePO_4$ materials, whereas it is the size effect (yielding stress relaxation) in $LiMnPO_4$ materials.[20] The difference between the two materials can probably be explained by the larger lattice misfit in $LiMnPO_4$, which also changes the nature of the transformation by modifying the crystallinity of the particles. An amorphization of $LiMnPO_4$ nanoparticles during the phase Li lithiation/delithiation transformation was reported by Meethong et al. from X-ray experiments.[20] They have also calculated that the critical size below which the amorphization occurs is 34 nm in $LiFePO_4$ and 78 nm in $LiMnPO_4$. In our particles, the particles are larger than 50 nm, which explains why no amorphous phase could be observed and that domino-cascade mechanisms seems to dominate the transformation.

In the future, it could be interesting to study a possible size effect in a system of partially discharged cells composed of heterogeneous particles to check if smaller particles lithiate first during discharge, as supposed by Lee et al.[40] Moreover, we think to extract the powders at the surface of an electrode by replica techniques and transfer them onto a TEM grid and analyze the entire surface of the grid with the automatic PED phase identification technique. Such observations could help discriminate between the bulk−core shell and the spinodal decomposition mesoscale models. We also think to use this technique to study a possible gradient of the $LiFePO_4/FePO_4$ proportion along the cell normal, from the electrolyte to the aluminum connector. A possible evolution of the tendency to form $LiFePO_4$ agglomerates and $FePO_4$ agglomerates during cycling will also be studied.

CONCLUSION

An automatic precession electron diffraction (PED) phase identification tool installed on a JEOL Model 2010-FEF TEM system operating at 200 kV has been used to obtain $LiFePO_4$ and $FePO_4$ phase maps at nanometer scale on a large number of

particles 50−300 nm in size in a partially charged cell. They clearly show that the particles are either fully lithiated or fully delithiated. The proportion of $LiFePO_4$ and $FePO_4$ phases, identified with the help of PED, is in good agreement with XRD measurements. The PED phase identification statistical results have been confirmed on a more-limited number of particles by careful "manual" TEM observations on an image Cs-corrected Titan Cube TEM system operating at 200 kV. The power spectra of HRTEM images of particles oriented along low-order zone axes have been indexed and the positions of the peaks have been used to discriminate the phases. Stacks of EFTEM images between −5 eV and 40 eV with a slit of 1 eV have been acquired and used to reconstruct the EELS spectra of different particles at their center and edges. All these experimental results confirm the validity of the domino-cascade model at the nanoscale level (the scale of the particles). Moreover, PED phase maps show that the larger particles are preferentially $FePO_4$, which suggest a size effect: larger particles are transformed by delithiation before the smaller ones. Such an effect could be explained by the importance of the elastic energy of the interface in large particles, which would accentuate the domino effect. A core−shell model or spinodal decomposition at mesoscale (scale of agglomerates of particles) is possible and will be studied in a future work. More generally, this study shows the importance of the PED phase mapping TEM attachment as a new technique to distinguish phases with very close lattice parameters and bring statistical information by phase mapping. We believe that the PED phase mapping technique will be used a standard tool in the future for battery applications and, more broadly, for applications involving multiphase nanomaterials.

AUTHOR INFORMATION

Corresponding Author

*Tel.: (+33) 04.38.78.93.29. Fax: (+33) 04.38.78.58.91. E-mail: cyril.cayron@cea.fr.

ACKNOWLEDGMENT

This work was supported by the French National Research Agency (ANR) through the "Recherche Technologique de Base" Program driven at the CEA/LETI by A. Chabli, by the ANR project AMOS, and by the CT206 UTTERMOST project in the framework of the European EUREKA/CATRENE program. We would like to thank S. Patoux, for his help in the electrochemical tests of the batteries, and A. Boulineau, for our discussions about electrochemistry of Li batteries.

REFERENCES

(1) Padhi, A. K.; Nanjundaswamy, K. S.; Goodenough, J. B. *J. Electrochem. Soc.* **1997**, *144*, 1188.
(2) Yamada, A.; Chung, S. C.; Hinokuna, K. *J. Electrochem. Soc.* **2001**, *148*, A224.
(3) Delacourt, C.; Poizot, P.; Levasseur, S.; Masquelier, C. *Electrochem. Solid State Lett.* **2006**, *9* (7), A352.
(4) Armand, M.; Gauthier, M.; Magnan, J. F.; Ravet, N. World Patent WO 02/27823 A1, 2002.
(5) Dominko, R.; Gaberscek, M.; Drofenik, J.; Bele, M.; Pejovnik, S. *Electrochem. Solid State Lett.* **2001**, *4*, A187.
(6) Chung, S. Y.; Bloking, J. T.; Chiang, Y. M. *Nature* **2002**, *1*, 1123.
(7) Islam, S. M.; Driscoll, F. J.; Fischer, C. A. J.; Slater, P. R. *Chem. Mater.* **2005**, *17*, 5085.
(8) Axmann, P.; Stinner, C.; Wohlfart-Mehrens, M.; Mauger, A.; Gendron, F.; Julien, C. M. *Chem. Mater.* **2009**, *21*, 1636.
(9) Kang, B.; Ceder, G. *Nature* **2009**, *458*, 190.
(10) Ceder, G.; Kang, B. *J. Power Sources* **2009**, *194*, 1024.
(11) Zaghib, K.; Dontigny, M.; Guerfi, A.; Charest, P.; Rodrigues, I.; Mauger, A.; Julien, C. M. *J. Power Sources* **2011**, *196*, 3949.
(12) Tang, P.; Holzwarth, N. A. W. *Phys. Rev. B* **2003**, *B68*, 165107.
(13) Morgan, D.; Ven, A. V. D.; Ceder, G. *Electrochem. Solid State Lett.* **2004**, *7* (2), A30.
(14) Chen, G.; Song, X.; Richardson, T. J. *Electrochem. Solid State Lett.* **2006**, *9*, A295.
(15) Ferrari, S.; Laval, R. L.; Capsoni, D.; Quartarone, E.; Magistris, A.; Mustarelli, P.; Canton, P. *J. Phys. Chem. C* **2010**, *114*, 12598.
(16) Andersson, A. S.; Kalska, B.; Häggström, L.; Thomas, J. O. *Solid State Ionics* **2000**, *130*, 41.
(17) Yamada, A.; Koizumi, H.; Sonoyama, N.; Kanno, R. *Electrochem. Solid State Lett.* **2005**, *8* (8), A409.
(18) Yamada, A.; Koizumi, H.; Nishimura, S. I.; Sonoyama, N.; Kanno, R.; Yonemura, T.; Kobayashi, O. *Nat. Mater.* **2006**, *5*, 357.
(19) Meethong, N.; Huang, H. Y. S.; Carter, W. C.; Chiang, Y. M. *Electrochem. Solid State Lett.* **2007**, *10* (5), A134.
(20) Meethong, N.; Kao, Y. H.; Huang, H. Y.; Carter, W. C.; Chiang, Y. M. *Chem. Mater.* **2008**, *20*, 6189.
(21) Kobayashi, G.; Nishimura, S. I.; Park, M. S.; Kanno, R.; Yashima, M.; Ida, T.; Yamada, A. *Adv. Funct. Mater.* **2009**, *19*, 395.
(22) Delacourt, C.; Poizot, P.; Tarascon, J. M.; Masquelier, C. *Nat. Mater.* **2005**, *4*, 254.
(23) Delacourt, C.; Rodriguez-Carjaval, J.; Schmitt, B.; Tarascon, J. M.; Masquelier, C. *Solid State Sci.* **2005**, *7*, 1506.
(24) Srinivasan, V.; Newman, J. *Electrochem. Solid State Lett.* **2006**, *9* (3), A110.
(25) Shin, H. C.; Chung, K. Y.; Min, W. S.; Byun, D. J.; Jang, H.; Cho, B. W. *Electrochem. Commun.* **2008**, *10*, 536.
(26) Laffont, L.; Delacourt, C.; Gibot, P.; Wu, M. Y.; Kooyman, P.; Masquelier, C.; Tarascon, J. M. *Chem. Mater.* **2006**, *18*, 5520.
(27) Delmas, C.; Maccario, M.; Croguennec, L.; Le Cras, F.; Weill, F. *Nat. Mater.* **2008**, *7*, 665.
(28) Meethong, N.; Huang, H. Y. S.; Speakman, S. A.; Carter, W. C.; Chiang, Y. M. *Adv. Funct. Mater.* **2007**, *17*, 1115.
(29) Ramana, C. V.; Mauger, A.; Gendron, F.; Julien, C. M.; Zaghib, K. *J. Power Sources* **2009**, *187*, 555.
(30) Zhang, W. J. *J. Power Sources* **2011**, *196*, 2962.
(31) Moreau, P.; Mauchamp, V.; Pailloux, F.; Boucher, F. *Appl. Phys. Lett.* **2009**, *94*, 123111.
(32) Martin, J. F.; Yamada, A.; Kobayashi, G.; Nishimura, S.; Kanno, R.; Guyomard, D.; Dupre, N. *Electrochem. Solid State Lett.* **2008**, *11*, A12.
(33) Rauch, E. F.; Dupuy, L. *Arch. Metall. Mater.* **2005**, *50*, 87.
(34) Rauch, E. F.; Duft, A. *Mater. Sci. Forum* **2005**, *495−497*, 197.
(35) Rauch, E. F.; Veron, M. *J. Mater. Sci. Eng. Technol.* **2005**, *36*, 552.
(36) Rauch, E. F.; Portillo, J.; Nicolopoulos, S.; Bultreys, D.; Rouvimov, S.; Moeck, P. *Z. Kristallogr.* **2010**, *225*, 103.
(37) *NanoMEGAS-CNRS patent pending technique*, www.nanomegas.com.
(38) Vincent, R.; Midgley, P. A. *Ultramicroscopy* **1994**, *53*, 271.
(39) Leriche, J. B.; Hamelet, S.; Shu, J.; Morcrettre, M.; Masquelier, C.; Ouvrard, G.; Zerrouki, M.; Soudan, P.; Belin, S.; Elkam, E.; Baudelet, F. *J. Electrochem. Soc.* **2010**, *157*, A606.
(40) Lee, K. T.; Kan, W. H.; Nazar, L. F. *J. Am. Chem. Soc.* **2009**, *131*, 6044.
(41) Jamnik, J.; Maier, J. *Phys. Chem. Chem. Phys.* **2003**, *5*, 5215.
(42) Plieth, W. J. *J. Phys. Chem.* **1982**, *86*, 3166.
(43) Wagermaker, M.; Mulder, F. M.; Van der Ven, A. *Adv. Mater.* **2009**, *21*, 2703.